



Influence of Full and Symmetrical Domains on the Numerical Flow around a SUBOFF Submarine Model using OpenFOAM

N. V. A. Permadi^{1†}, J. H. Chen¹ and E. Sugiarto²

¹ Department of Systems & Naval Mechatronic Engineering, National Cheng Kung University, Tainan, Taiwan

² Department of Marine Engineering, Hang Tuah University, Surabaya, Indonesia

†Corresponding Author Email: p16107025@gs.ncku.edu.tw

(Received August 31, 2022; accepted January 19, 2023)

ABSTRACT

In this research, we consider the influence of two kinds of domain on the numerical flow around a submarine model. A fully appended SUBOFF submarine model was used, and the structure and characteristics of the flow were investigated under a full domain and a symmetrical domain arrangement. The numerical simulation was carried out using the OpenFOAM software, and the flow was numerically modelled as single-phase and incompressible. The SST $k-\omega$ turbulence model was used in both domains, together with an insensitive Spalding wall function to represent the boundary layer near the wall. The results showed that simulations in both the full and symmetrical domains could accurately predict the total resistance. Compared to the symmetrical domain, the resistance value obtained with the full domain was more precise; the symmetrical domain under coarse grid conditions had an error value of 1.34%, whereas the full domain using the same grid size had an error value of 0.6%. Hence, the full domain was superior in terms of predicting the resistance with a coarse grid. Next, the pressure coefficient comparison at the leading edge of the rudder was calculated, where $x/L=0.92$, and the symmetric domain was found to have a value of 0.0747 whereas the full domain had a value of 0.236. Compared with the results from experiment ($C_p=0.302$), the symmetric domain appears to give an underestimate for the pressure distribution at this position. In addition, the flow structures and properties in both domains differ, particularly in terms of the vortical structures generated by the sail and rudders. The simulation results for the full domain reveal that the flow around the SUBOFF model is asymmetric. The full domain was able to capture the flow structures in more detail than the symmetrical domain, and represented the velocity distribution at the propeller plane better. As a result, the full domain must be considered when carrying out propeller analysis and self-propulsion simulations.

Keywords: Turbulent flow; Wall function; Velocity distribution; Stern wake; Flow structures; Numerical accuracy; OpenFOAM.

NOMENCLATURE

C_f	friction coefficient	ω	specific dissipation rate
C_p	pressure coefficient	p	dynamic pressure
D	diameter of hull	RT	total resistance
Δ	displacement	ρ	fluid density
GCI	grid convergence index	S	wetted surface area
k	turbulence kinetic energy	T	draught
L	ship length	U	velocity field
μ_t	turbulence viscosity	U_o	free stream velocity

1. INTRODUCTION

The flow past a rigid body can be solved by computational fluid dynamics (CFD), which allows

us to predict the characteristics of a fluid flow passing through a body. The flow past a cylinder is considered to be a classical body problem in fluid mechanics. The problem is taken into consideration

as the basic understanding in fluid mechanics application, although the cylinder model is simple. The most important quantity associated with the flow past a cylinder is the drag coefficient. Various studies have been conducted in which CFD has been applied to the cylinder model. [Catalano *et al.* \(2003\)](#) investigated turbulent flows by running a large-eddy simulation (LES) with wall modelling around a circular cylinder at high Reynolds number. The results were compared with the steady and unsteady solutions obtained from RANS as well as with experimental data. The results proved the accuracy of the LES better than the RANS solutions. The method proposed in their study was able to capture the boundary layer separation correctly. A similar study was performed using the partial Navier-Stokes equations (PANS), and the results confirmed the ability of PANS, when combined with the turbulent kinetic energy fraction, $f_k < 0.05$, to reduce the numerical error compared with the case where $f_k = 1$ ([Pereira *et al.* 2018](#)). [Rajani *et al.* \(2009\)](#) used RANS3D, a second-order implicit finite volume Navier-Stokes solver, to simulate laminar flow past 2D and 3D circular cylinders. Their research aimed to investigate the mean surface pressure, skin friction coefficient, wake recirculation strength in the steady flow regime, and vortex shedding in the unsteady flow regime. Their simulation results agreed well with the corresponding measurement data for the 2D case; however, the flow simulation for a 3D circular cylinder showed instability at the critical Reynolds number of 180.

[Pantokratoras \(2017\)](#) conducted a study of a steady flow of power-law fluid across a circular rotating cylinder, with varying values of the Reynolds number and rotation rate, to investigate the lift and drag forces acting on the rotating cylinder under non-Newtonian flow. Their results proved that for all kinds of fluids, the lift coefficient increased either linearly or nonlinearly with increasing rotation, whereas the drag coefficient was slightly affected by rotation at low Reynolds numbers but decreased with an increase in the rotation rate. The flow past a circular cylinder becomes more complex when the geometry is changed to a finite 3D shape, and in this case, 3D flow solvers must be applied. [Gao *et al.* \(2018\)](#) numerically investigated the flow around a finite circular cylinder with two free ends in order to demonstrate how the flow pattern and turbulent structure change with geometry aspect ratio and Reynolds number. Their investigation confirmed that, when compared to the 2D model, the drag coefficient decreased dramatically and the pressure distribution over the back of the circular cylinder increased. Furthermore, the flow structure around a finite circular cylinder with two ends differed significantly from that of an infinite cylinder or a finite circular cylinder with one free end. From the various studies in this area, it can be seen that the characteristics of the flow passing a 2D or 3D circular cylinder are complex and unique. Although the profile shapes of 2D and 3D circular cylinders are the same, there is a discrepancy in the flow characteristics between these cases.

Other studies conducted by [Yin and Ong \(2020\)](#),

[Constantinescu and Squires \(2004\)](#), [Sadikin *et al.* \(2014\)](#), and [Yen *et al.* \(2017\)](#) demonstrated that the flow past a solid sphere differs from the flow past a circular cylinder, especially in terms of vortex shedding in the wake flow behind the sphere.

In the past, numerical analysis studies were performed in order to reach a comprehensive understanding of the flow past a simple body before applying the method to a more complex geometry. Nowadays, CFD is a more reliable method of analysing the hydrodynamics of a complex geometry such as a ship (both free surface ships and submarines), and many kinds of CFD approaches have been applied ([Sugianto *et al.* 2022](#); [Permadi and Sugianto 2022](#)). [Atta *et al.* \(2019\)](#) used CFD to perform a hydrodynamic design and performance analysis of underwater vehicles. The steady state RANS method was used to investigate the effects of the model's wall roughness, linear velocity, and rotation speed on its hydrodynamic performance. The results were used to optimise the design. A CFD validation experiment was conducted by [Toxopeus \(2008\)](#) on a bare hull form of the SUBOFF model, which showed good agreement with the experimental data for local fields and global quantities.

[Pan *et al.* \(2012\)](#) predicted the hydrodynamic coefficient of a SUBOFF submarine model using CFD simulation. Steady and unsteady RANS models were employed in the study. In addition, the planar motion mechanism (PMM) was simulated using a dynamic mesh method. Their approach could be successfully applied to solve for the flow around the submarine model as well as its motion. The accuracy of their method was found to be acceptable when compared with the experimental results.

A hydrodynamic investigation of a SUBOFF submarine model under free surface flow was carried out by [Doğrul \(2019\)](#). The free surface effects were taken into account at different Reynolds numbers and different depths. An unsteady RANS model combined with $k-\epsilon$ was applied in the study. The results showed that the submergence depth had a significant effect on the resistance components for Froude numbers larger than 0.7, and that the appendages had less effect on the free surface transformation at all depths.

[Takahashi and Sahoo \(2019\)](#) examined the potential of CFD in terms of estimating the hydrodynamic performance of submarines at the model scale. A SUBOFF model was used in their study. The hull translation and drift were simulated, and the results were validated against another published methodology and procedure. It was found that the resistance in the velocity function was consistent with the experimental data. Overall, the motion forces and moments showed the same behaviour as in the experimental results, although the sway force and yawing moment showed significant differences.

[Lungu \(2019\)](#) applied a different CFD approach using a detached eddy simulation (DES) to simulate the flow around a SUBOFF model. To verify and validate the numerical results, a grid convergence

test was performed. Despite its high computational cost, the DES method used in their study was able to capture the details of the flow around the model. Using OpenFOAM, Paredes *et al.* (2021) characterized the numerical flow around a Type 209 submarine. Prior to applying it to the Type 209 submarine, a multiphase solver was chosen and validated using a SUBOFF model. According to the findings, the bow had a high velocity gradient, pressure fluctuations, and large turbulent vortical structures. A multi-zone fluid domain with sliding mesh was used in another approach to the hydrodynamic analysis of a SUBOFF model. Menter's shear stress transport (SST) k-turbulence model was combined with an unsteady RANS model (Lin and Li 2020). The usefulness of a sliding mesh in terms of analysing the hydrodynamic characteristics, vorticity, frictional coefficient, and pressure coefficient was demonstrated in their study.

All of the works described above applied CFD to either a simple or complex model; however, the focus in each case was on the estimation of global quantities using numerical approaches, without describing the detailed effects of the computational domain arrangement on the structure of the flow past a body. In the present study, the influence of the use of a full domain and a symmetrical domain on the numerical flow around a SUBOFF submarine model are investigated. The configuration of the model includes all the appendages, consisting of a sail and four rudders. Although the bare hull of this model is axisymmetric, the addition of the appendages means that the model is only symmetrical in one plane. The flow around the submarine may be dominated by vortical structures, particularly in the regions near the sail and rudders. The shedding flow structures downstream of the hull when the vehicle is moving straight ahead may also be unique. Hence, a feasible computational domain arrangement needs to be considered when numerical analysis is used to solve for the flow around the submarine.

In this study, we investigate the effects of the type of computational domain, specifically a full domain and a symmetrical domain, on the numerical flow around the model. Both approaches' results are compared and validated against experimental data and previous work. In addition, the behaviour of the simulation on the full and symmetrical domains is verified using uncertainty analysis.

2. NUMERICAL APPROXIMATION

2.1 Geometry

A fully appended SUBOFF submarine model (configuration AFF-8) was used in the numerical simulation. The hull was appended with a sail and four rudders, installed at the stern of the body. The model in this configuration is illustrated in Fig. 1. As experimental data, a speed of 5.93 knots was used in the numerical simulation. Table 1 shows the main parameters of the SUBOFF model.

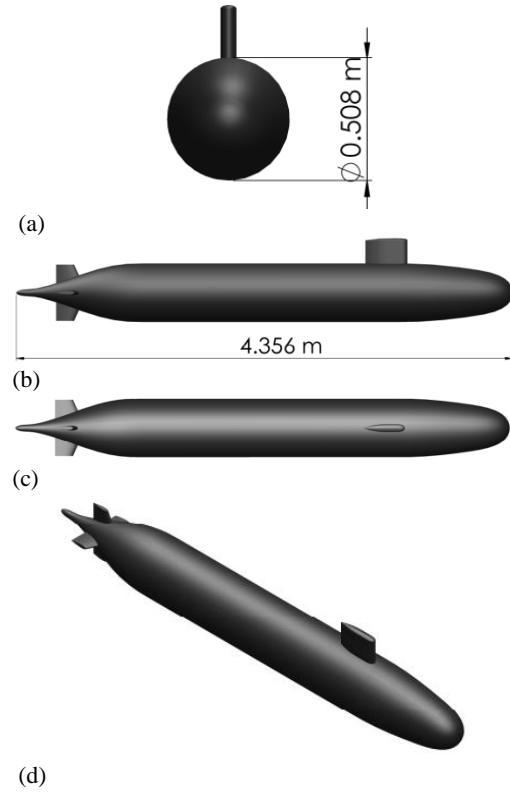


Fig. 1. SUBOFF model with full appendages: (a) front view; (b) side view; (c) top view; (d) isometric view.

Table 1 Main parameters of the scaled SUBOFF model.

Parameter	Symbol	Value
Length [m]	L	4.356
Length-diameter ratio	L/D	8.575
Draft-diameter ratio	T/D	0.863
Length percentage of fore body	L_{FB}/L	0.233
Length percentage of parallel middle body	L_{PMB}/L	0.512
Length percentage of aft body	L_{AB}/L	0.255
Relative sail location	L_{FC}/L	0.21
Wetted area of hull at surface [m ²]	S_{surf}	4.760
Wetted area of hull + sail [m ²]	$S_{hull} - S_{sail}$	6.160
Wetted surface area of sail [m ²]	S_{sail}	0.184
Displacement at surface condition [tons]	Δ_{surf}	0.650
Displacement submerge hull + sail [tons]	Δ_{sub}	0.703

2.2 Governing Equation

The water flow around the hull was modelled using OpenFOAM v2112 as a steady-state, single-phase, incompressible flow. The governing equation of the flow can be expressed using the incompressible RANS, as shown in the following equations.

Continuity equation:

$$\frac{\partial(u_i)}{\partial x_i} = 0 \quad (1)$$

Momentum equation:

$$\rho u_j \frac{\partial(u_i)}{\partial x_j} = \rho F_i - \frac{\partial P}{\partial x_i} + \frac{\partial}{\partial x_j} (\rho \overline{u'_i u'_j}) \quad (2)$$

where u_i is the time-averaged velocity component in Cartesian coordinates $x_i (i = 1, 2, 3, \dots)$, ρ is the density of the fluid, F_i are the body forces, P is the time-averaged pressure, μ is the viscous coefficient, u'_i are the fluctuating velocity components in Cartesian coordinates, and $-\rho \overline{u'_i u'_j}$ is the Reynolds stress tensor. This value can be computed based on the Boussinesq hypothesis (Ueda and Hinze 1975), which is given as:

$$-\rho \overline{u'_i u'_j} = \frac{\mu_t \partial u_i}{\partial x_j} + \frac{\partial u_j}{\partial x_i} - \frac{2}{3} \left(\rho k + \frac{\mu_t \partial u_k}{\partial x_k} \right) \delta_{ij} \quad (3)$$

where μ_t and k are the eddy viscosity and turbulent kinetic energy, respectively. The hypothesis is applicable to the k -SST turbulence model (Menter 1994). This turbulence model was employed in this study due to its capability to treat the pressure gradient and flow separation. In addition, the Spalding turbulence wall function was proposed to capture the boundary layer within the computational domain. The equation for the $k - \omega$ SST model is as follows:

$$\frac{\partial(\rho k u_i)}{\partial x_i} = \partial \left(\frac{\Gamma_k \partial k}{\partial x_i} \right) + G_k - Y - k + S_k \quad (4)$$

$$\frac{\partial(\rho \omega u_i)}{\partial x_i} = \partial \left(\frac{\Gamma_\omega \partial \omega}{\partial x_j} \right) + G_\omega - Y_\omega + D_\omega + S_k \quad (5)$$

where:

G_k is the generation of turbulent kinetic energy k as a result of the mean velocity gradient;

G_ω is the generation of the specific dissipation rate as a result of the mean velocity gradient;

Γ_k, Γ_ω are the effective diffusion coefficients of k and ω ;

Y_k, Y_ω are the dissipation rate due to turbulence;

D_ω is the dissipation of k and ω due to turbulence;

D_ω is the cross-diffusion term;

S_k are the undefined source terms.

The governing equation was discretised using the finite volume method (FVM). In this research, to discretize the convective terms and turbulence quantity, the semi-implicit method for pressure-linked equations-consistent (SIMPLEC) was used, and a second-order upwind scheme was chosen (Barth and Jespersen 1989). The diffusive term was discretized using a second-order central difference scheme (Ellis *et al.* 2016; Pook *et al.* 2018).

2.3 Computational Domain

The computational domain size was determined in accordance with the ITTC guidelines (Versteeg and Malalsekera 2007; ITTC 2011), and both the full and symmetrical domains were defined following these guidelines. As shown in Fig. 2, the inlet, outlet, and wall boundaries were set with sufficient distance from the model. The dimensions are defined in relation to the model's length, with $3L$ being the space between the reference coordinates and the inlet side, and $4L$ being the space between the reference coordinates and the outlet side. The space between the midplane and the far-field side was $2.5L$, except that in the full domain, it was appended with the same size in the opposite direction. The distance between the centreline of the hull and the bottom of computational domain was $2L$, whereas $1L$ was the space to the top side. Table 2 summarizes the boundary conditions for each fluid quantity in the full and symmetrical domains. In accordance with the initial conditions, the incoming flow was initialised with the model speed at a Froude number of 0.467. In addition, the kinetic energy of turbulence k and dissipation rate ω were set based on the assumption that the turbulence intensity level

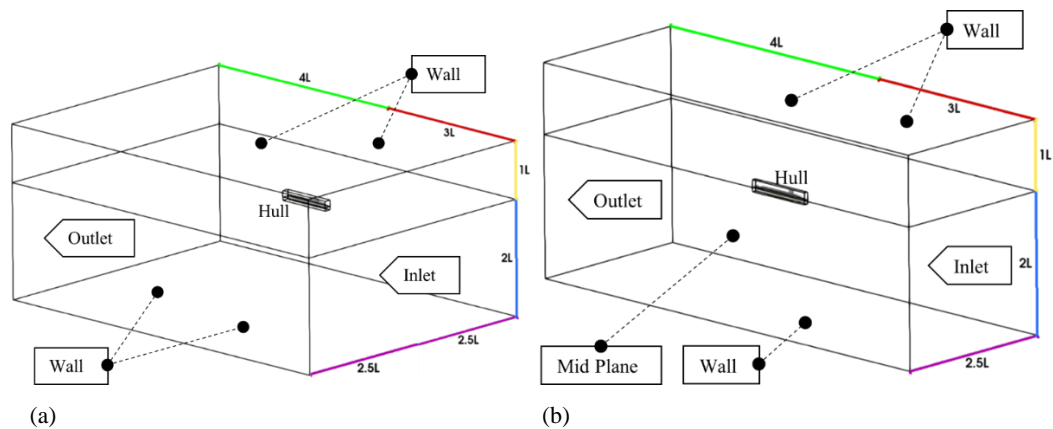


Fig. 2. Computational domain and boundaries imposed in the SUBOFF model: (a) full domain mesh; (b) symmetrical domain mesh.

Table 2 Names and conditions of boundaries.

Domain type	Boundary name	Boundary conditions	
		U	p
Full	Inlet	fixedValue	zeroGradient
	Outlet	inletOutlet	fixedValue
	Wall	noSlip	zeroGradient
	Hull	noSlip	zeroGradient
Symmetric	Inlet	fixedValue	zeroGradient
	Outlet	inletOutlet	fixedValue
	Wall	noSlip	zeroGradient
	Mid plane	symmetryPlane	symmetryPlane
	Hull	noSlip	zeroGradient

was low. The Spalding wall function was then applied to solve for the flow in the boundary layer.

2.3 Mesh Generation

The mesh used in the computational domain was a structured mesh with hex-dominant cells. The cell size within the domain was refined at several levels, especially near the hull. The mesh was constructed in stages. First, a hexahedral grid was created with *blockMesh* as a background mesh for the free stream flow. Then, four refinement levels were applied using the *topoSet* tool to gradually increase the density of the mesh for the elements closer to the model. The background mesh was then subtracted from the model using the *snappyHexMesh* dictionary. The surface of the model was refined at level 2 to ensure smooth snapping of the background mesh. In order to achieve the y^+ target, the final meshing process involved adding six prismatic layers parallel to the hull with an expansion ratio of 1.15. The first layer centroid was considered at a value of y^+ of 45. This was done because the y^+ insensitive wall function is applied in the $k - \omega$ SST turbulence model. This involves a near-wall treatment which requires at least five to 10 layers,

with the centroid of the first cell placed with a y^+ value of between 40 and 50. The final mesh is illustrated in Fig. 3(a) and Fig. 3(b), and the prismatic layer near the wall is shown in Fig. 4(a) and Fig. 4(b).

2.4 Verification and Validation

To estimate the uncertainty in the simulation results, verification and validation were performed. Verification is used to evaluate a numerical solver's consistency, whereas validation is an assessment of its accuracy (ITTC 2017). A numerical simulation occasionally introduces some errors and uncertainties, as the calculations are based on approximations, and verification and validation are important in order to evaluate these uncertainties. The errors and uncertainties are directly defined following those used in the experimental uncertainty analysis. The ITTC has defined the simulation error δ_S as the difference between the simulation result S and the truth T . It is composed of the additive modelling error δ_{SM} and numerical error δ_{SN} in CFD ($\delta_S = S - T = \delta_{SM} + \delta_{SN}$). For specific conditions, the sign and magnitude of the numerical error can be

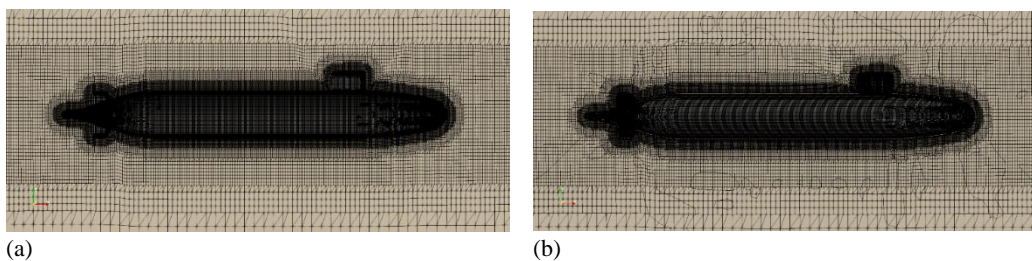


Fig. 3. Final generated mesh: (a) full domain mesh; (b) symmetrical domain mesh.

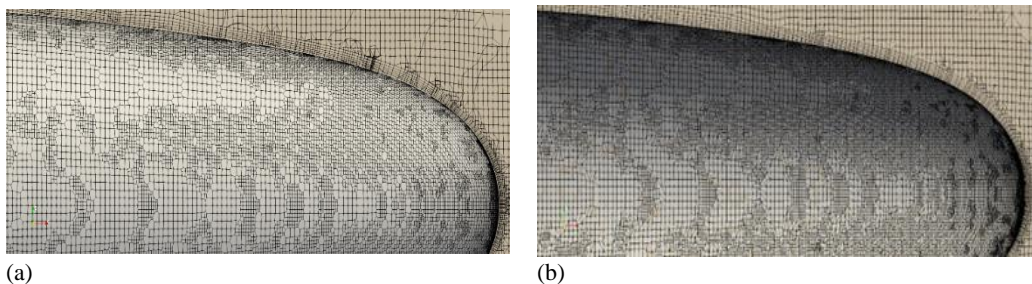


Fig. 4. Prismatic layers near the wall: (a) full domain; (b) symmetrical domain.

approximated as $\delta_{SN} = \delta_{SN}^* + \varepsilon_{SN}$, where δ_{SN}^* is a magnitude approximation of numerical inaccuracy and ε_{SN} is the error in that approximation. The simulation value is corrected to provide a numerical benchmark S_c , which is expressed as $S_c = S - \delta_{SN}^*$.

Verification is used to assess the numerical uncertainty U_{SN} and to estimate the sign of the error in the magnitude δ_{SN}^* of the numerical result, when conditions permit. In addition, it allows us to assess the uncertainty in the error estimation U_{SCN} . In the uncorrected simulation approach, the numerical error is decomposed into the contributions from the iteration number δ_I , grid size δ_G , time step δ_T , and other parameters δ_P . The numerical uncertainty is expressed as:

$$U_{SN}^2 = U_I^2 + U_G^2 + U_T^2 + U_P^2 \quad (6)$$

In the corrected simulation method, the solution is adjusted to yield a numerical benchmark S_c where the estimated simulation numerical error δ_{SN}^* and corrected uncertainty U_{SCN} are given by:

$$\delta_{SN}^* = \delta_I^* + \delta_G^* + \delta_T^* + \delta_P^* \quad (7)$$

$$U_{SCN}^2 = U_{IC}^2 + U_{GC}^2 + U_{TC}^2 + U_{PC}^2 \quad (8)$$

Validation is applied to evaluate the simulation modelling uncertainty U_{SM} by data of experimental benchmark, where conditions allow, to approximate the magnitude of the modelling inaccuracy δ_{SM} . The error E is obtained from the inequality between the simulation values S and data D :

$$E = D - S = \delta_D - (\delta_{SM} + \delta_{SN}) \quad (9)$$

The modelling error δ_{SM} can be formulated into modelling assumptions and previous data using. In order to decide whether validation has been accomplished, E is compared to the validation uncertainty U_V , defined by:

$$U_V^2 = U_D^2 + U_{SN}^2 \quad (10)$$

If $|E| < U_V$, the combination of all errors in D and S is smaller than U_V , and validation has been achieved at the U_V level. If $U_V \ll |E|$, the sign and magnitude of $E \approx \delta_{SM}$ can be used to make improvements to the model. For the corrected simulations, the equations can be represented as:

$$E = D - S_c = \delta_D - (\delta_{SM} + \delta_{SN}) \quad (11)$$

$$U_{Vc}^2 = U_{Ec}^2 - U_{SM}^2 = U_D^2 + U_{SCN}^2 \quad (12)$$

Since modelling errors are very difficult to quantify, only the numerical errors in the simulation are given attention. According to the ITTC guidelines, errors related to the iteration, the grid, and the time step are investigated by varying specific conditions while leaving the other parameters unchanged. As a result, the majority of the uncertainties in the grid size and time step can be examined.

Numerical uncertainty is frequently introduced during CFD simulations. It includes the accuracy

effects of the discretisation scheme and the rounding and iterative convergence errors (Roy 2005). Grid refinement based on a grid convergence index (GCI) is the most feasible solution to numerical uncertainties (Paudel and Saenger 2017; Boache 1994). Essentially, the GCI is used to analyze solutions obtained from various grid size, and determines the significance of the changes in the numerical solution due to a higher grid refinement (Roache 1998). A refinement process is used to generate several solutions (at most three) for the variable under investigation while all other variables remain constant. The grid spacing of the full and symmetrical domain meshes was varied in this study with a specific refinement ratio r_i . A value of $r_i = \sqrt{2}$ was adopted, as it has a relatively high parameter refinement ratio and allows the coarse-solution to be extended as a starting point for the fine-solution. The transition from medium to fine $\varepsilon_{i,21} = \hat{S}_{i,2} - \hat{S}_{i,1}$ and coarse to medium $\varepsilon_{i,32} = \hat{S}_{i,3} - \hat{S}_{i,2}$ solutions is utilised to define the convergence ratio $R_i = \varepsilon_{i,21}/\varepsilon_{i,32}$, where $\hat{S}_{i,1}, \hat{S}_{i,2}, \hat{S}_{i,3}$ are the solutions for the fine, medium, and coarse input parameters, respectively (Islam and Soares 2019). For each mesh, the total resistance at a speed of 5.93 knots was used as the solution. Three convergence conditions are possible based on the value of R_i :

- (1) Monotonic convergence: $0 < R_i < 1$
- (2) Oscillatory convergence: $R_i < 0$
- (3) Divergence: $R_i > 1$

The Richardson extrapolation is carried out to estimate U_I or δ_I^* and U_{IC} for monotonic convergence. For oscillatory convergence, the uncertainties are approximated by limiting the error to the average of the oscillating maximum (S_U) and minimum (S_L), $U_I = \frac{1}{2} \left(\frac{S_U}{S_L} \right)$. The errors and uncertainties cannot be approximated under the divergence condition.

3. RESULTS AND DISCUSSION

3.1 Grid Independence Analysis

The iterative convergence prescribed for the numerical solutions in this study is a maximum normalised residual and force quantities (Rocha *et al.* 2017). A grid independence analysis was carried out to assess the numerical uncertainty for different numbers of cells in the computational domain. Three types of mesh were generated for both computational domains (full and symmetrical domains), in order to determine the grid independence and GCI. Table 3 shows the total number of cells for the three types of mesh. The number of cells generated in the symmetrical domain was maintained in such way that the value was approximately half the number of cells in the full domain. The grid density was increased from coarse to fine by reducing the cell size only in the x -direction, with a refinement ratio $r_i = \sqrt{2}$, without modifying the cell size in the other directions. The solutions achieved from both domains were

Table 3. Types of mesh and numbers of cells.

Domain type	Grid density	Number of cells
Symmetric	Coarse	911,249
	Medium	1,267,959
	Fine	1,800,313
Full	Coarse	1,846,432
	Medium	2,574,485
	Fine	3,657,842

compared and evaluated in terms of their numerical uncertainty.

Figure 5 shows the evolution of the normalised residual for the momentum and turbulence properties. In this study, the convergence criterion was set as all residuals dropping to the power of 10^{-5} . However, in order to confirm the convergence, the value of a physical quantity such as force was also probed, as shown in Fig. 6. From the results, it can be seen that all residuals smoothly decreased to the power of 10^{-5} . In addition, the evolution of the value of the force over the iterations indicated convergence.

Grid convergence was consistent for all mesh types in both the full and symmetrical domains. Figure 7 represents the evolution in the resistance force for all grids. It can be seen from Fig. 7(a) that the solutions for the full computational domain reached convergence after 150 iterations, whereas Fig. 7(b) shows that convergence was achieved after 200 iterations for the symmetrical domain. The execution time in the symmetrical domain was much faster than in the full domain, since the total number of cells in

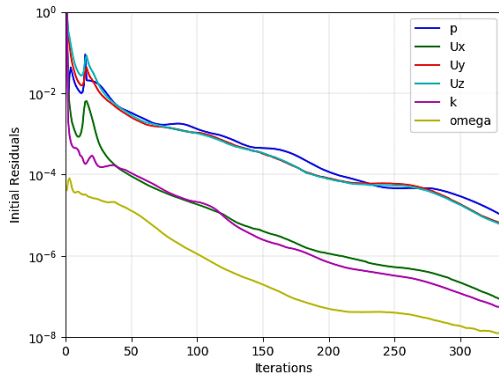


Fig. 5. Evolution in the residuals with iteration.

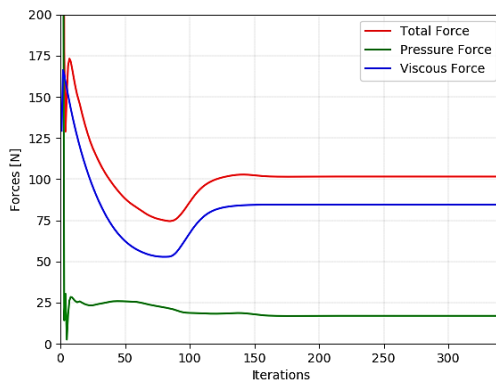


Fig. 6. Evolution in the force quantities with iteration.

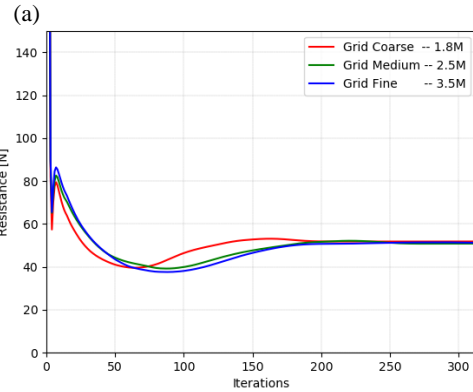
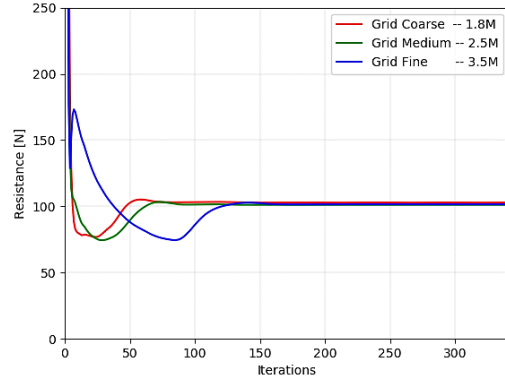


Fig. 7. Grid convergence of the forces on the SUBOFF model in (a) the full domain and (b) the symmetrical domain.

the symmetrical domain was only about half of that in the full domain. However, a longer iterative process was needed to achieve convergence in the symmetrical domain.

The total resistance for the symmetrical domain was obtained by multiplying the total force by two. In order to assess the accuracy for both computational domains, the resistance values were compared with experimental data reported by Huang *et al.* (1992). This comparison was extended to an uncertainty analysis in which the numerical errors given by each grid type were evaluated. Table 4 shows a comparison of the solutions, and Table 5 presents the results of mesh uncertainty.

From the results, we see that the R_i magnitudes for both computational domains exhibit monotonic convergence, and the order of accuracy (P_i) can be expressed using the equation below (ITTC 2017):

$$P_i = \frac{\ln(\varepsilon_{i,32}/\varepsilon_{i,21})}{\ln(r_i)} \quad (13)$$

The GCI for the grid independence test of total resistance over two grid solutions can be calculated by the following equation (Lin and Li 2020):

$$GCI = \frac{F_s}{r_i^{P_i}} \left| \frac{\hat{S}_{i+1} - \hat{S}_i}{\hat{S}_i} \right| \quad (14)$$

where F_s is a safety factor and 95% confidence is implied for the uncertainty estimate (Boache 1994). A value of $F_s = 1.25$ has been suggested for use with such grids (Roache 1997). Since all GCI values

Table 4 Comparison of resistance.

Domain type	Grid density	Resistance [N]		Error (%)
		CFD	Exp.	
Symmetric	Fine	103.67	102.39	0.60
	Medium	101.81		0.70
	Coarse	101.63		0.71
Full	Fine	102.91	102.39	1.34
	Medium	101.58		0.48
	Coarse	101.57		0.66

Table 5 Result of mesh uncertainty.

Domain type	Grid density	No. of cells	$\hat{S}_i n(RT)$	$\epsilon_{i,21}$	$\epsilon_{i,32}$	R_i	P_i	GCI_{21}	GCI_{32}
Symmetric	Fine	1,800,313	101.63	0.18	2.06	0.087	7.03	1.9×10^{-4}	2×10^{-3}
	Medium	1,267,959	101.81						
	Coarse	911,249	103.67						
Full	Fine	3,657,842	101.57	0.01	1.33	0.008	14.11	9.3×10^{-7}	1.4×10^{-3}
	Medium	2,574,485	101.58						
	Coarse	1,846,432	102.91						

were below 1.5% (Roache 1998), we have verification that the results represented a grid-independent solution.

3.2 Analysis of Flow Characteristics

Figures 8(a) and (b) show the vorticity distribution around the SUBOFF model on both the full and the symmetrical domains. The results show the difference in the vorticity distribution between the two domains. When viewing these from the propeller plane, we see that although the magnitudes of the vorticity are identical, the structures are dissimilar. The full domain exhibits asymmetrical results in terms of the vorticity distribution, due to the boundary conditions which were imposed on both the left and the right sides of the far-field faces. As a result, the actual flow around the hull is not completely symmetric. This is different from the symmetrical domain, in which the midplane was considered to be the plane of symmetry. Hence, the

boundary condition imposed at the face of the symmetric plane resulted in symmetric flow due to reflection.

Figures 9(a) and (b) depict the vorticity structures and their distribution around the hull of the SUBOFF model. From the results, it is obvious that the vortex at the top of the water sail is convected downstream. This convection is captured accurately by the full domain model, unlike in the symmetrical model. Furthermore, as the boundary layer thickened, the vortices that separated from the sail were convected to the stern and amplified. The inflow field behind the rudders is significantly non-uniform, as all the vortical structures interact with each other.

Next, the isosurfaces were computed to allow us to visualise and compare the local flow structures in the full and symmetrical domains. The isosurfaces obtained for the full domain are presented in Fig. 10(a), and the results for the symmetrical domain in Fig. 10(b).

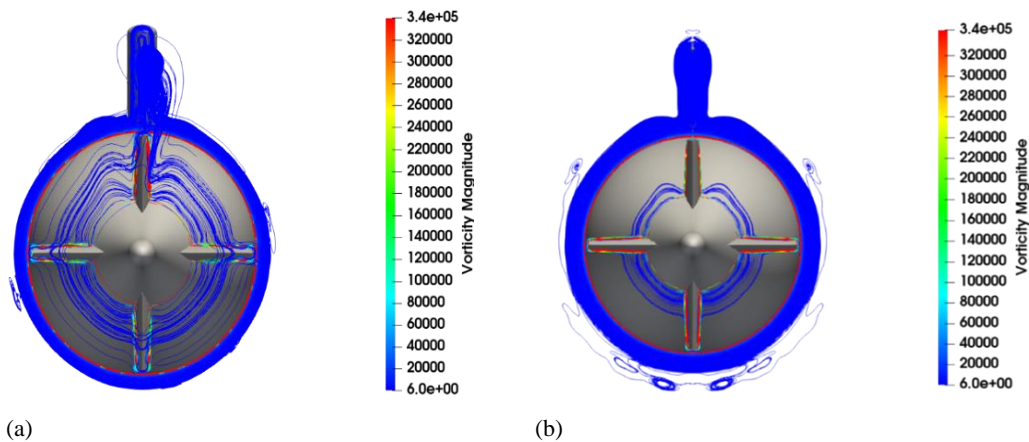
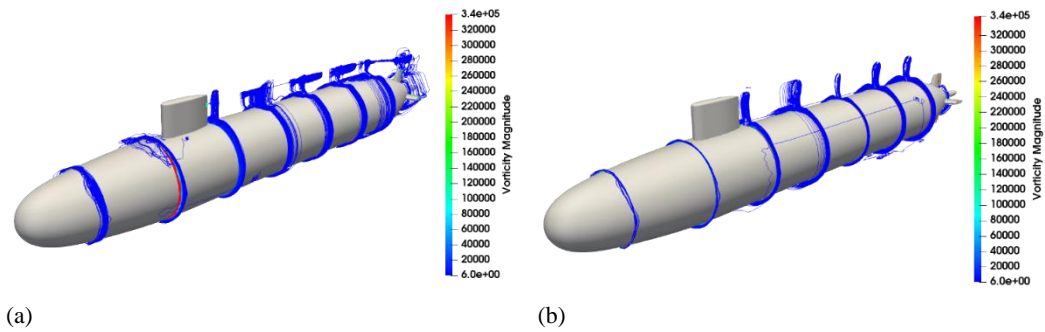
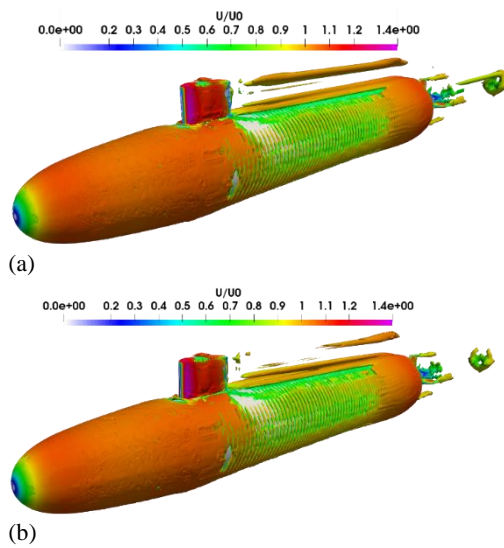


Fig. 8. Magnitude and distribution of the vorticity, as viewed from the propeller plane: (a) full domain; (b) symmetrical domain.



(a) (b)
Fig. 9. Magnitude and distribution of the vorticity around the hull of the SUBOFF model: (a) full domain; (b) symmetrical domain.

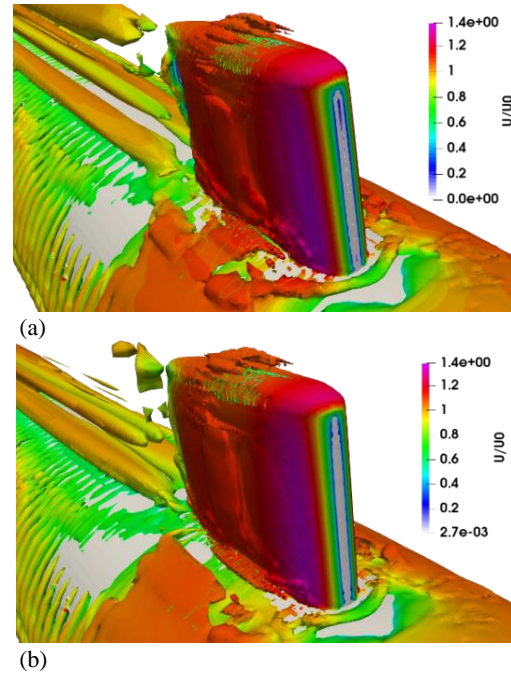


(a) (b)
Fig. 10. Comparison between isosurfaces in (a) the full domain; (b) the symmetrical domain.

The images are coloured based on the velocity. Although the full domain solutions were more expensive in terms of computational time, it was found that these better captured the development of the wake of the appended hull, and in particular, the flow structures were continuously captured in the full domain. This can be an important issue which significantly affects the self-propulsion when it is analysed using numerical simulation, as the nominal wake can strongly influence the performance of the propeller. The vortices generated by the tip of the sail and rudders in the full domain are asymmetric, thus proving the accuracy of the full computational domain. From the results, it can be observed that the flow passing through the sail to the wake region was captured in detail. Although the number of cells in the symmetrical domain was set to half of that in the full domain, with the same refinement ratio, the symmetrical domain seemed to have deficiencies in capturing the detailed flow structures along the hull.

However, both computational domains were able to accurately depict the horseshoe vortex near the root of the sail, as shown in Figs. 11(a) and (b). Although less intense than the vortices formed at the tip, the significant pressure gradient at the junction of the hull and the appendages must be considered.

The velocity profile around the hull exhibited a sharp



(a) (b)
Fig. 11. Horseshoe vortex in front of the sail in (a) the full domain; (b) the symmetrical domain.

gradient. When an incoming flow comes into contact with a sharp object, the flow will separate as a consequence of the blocking effect. This divided flow generates multiple vortices around the body, which have a similar appearance to the horseshoe vortices generated around a junction. The flow becomes increasingly intricate when the vortices contact with the boundary layer formed close to the body. This complicated flow can be observed in a variety of places, including the flow around appendages.

In addition to the flow structures due to the sail, the tip vortices at the four rudders were also well captured in the full domain, unlike in the symmetrical domain. A comparison of the tip vortices generated in the full and symmetrical domains is presented in Fig. 12.

The full domain mesh was able to generate the actual structures in the local flow. Due to the presence of the sail and four rudders, the flow around the SUBOFF model is not perfectly symmetric. Despite the fact that the hull is symmetric about the midplane, the fluid flow computed by numerical

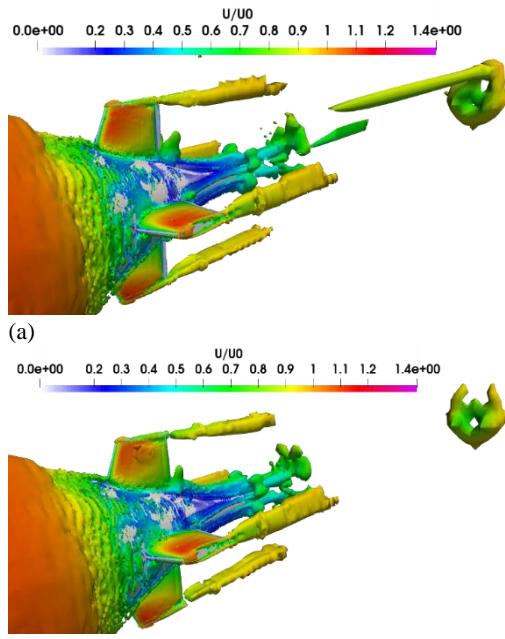


Fig. 12. Tip vortices at the four rudders captured in (a) the full domain; (b) the symmetrical domain.

simulation exhibited asymmetric behaviour, as illustrated in the results for the full domain.

Figures 13(a) and 13(b) show the normalised velocity distributions on the propeller plane in both domains. It can be seen that the velocity distributions

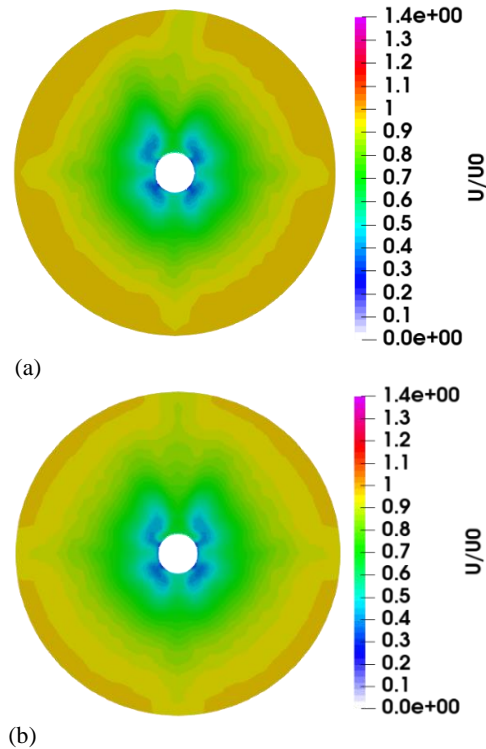


Fig. 13. Velocity distribution at the propeller plane in (a) the full domain; (b) the symmetrical domain.

differ between the computational domains. Since the wake generated by the sail varies between the domains, this influences the nominal wake distribution, especially at the stern. As a result, the velocity distribution at the propeller plane differs between the full and symmetrical domains in several ways. The magnitude of the velocity distribution at the propeller disc in the full domain is greater than that in the symmetrical domain, but the distribution is not uniform, as can be seen from Fig. 12(a). Higher magnitudes are more concentrated to the right of the propeller plane. Both domains exhibit the same velocity distribution behaviour at the top of the propeller axis. The results show that the magnitude of the velocity is greater in that location due to the vorticity of the sail, which is convected to the propeller plane. As a result, the velocity downstream to the stern is magnified.

Figure 14 depicts the friction coefficient C_f for the SUBOFF model along the upper meridian line. The C_f values obtained in the present study for the full and symmetrical domains are compared with experimental results and those of other numerical simulations (Qiu *et al.* 2007).

Both results showed comparable behaviour. Due to the contact between the boundary layer flows and the leading edges of the appendages, local peaks in C_f were observed before the sail and rudders. The drop in C_f from the sail's top was accompanied by the formation of a tip vortex that moved downstream. Consequently, C_f will drop due to the interaction of the boundary separation with the shear layers from the hull and rudders.

Figures 15(a) and 15(b) show the pressure coefficient distributions for the SUBOFF models. As predicted, high-pressure zones can be found around the nose of the bow as well as each appendage. Regions of minimal pressure are identified along the lateral sides of the sail and rudders, and at the hull within the region where its size starts to decline. It is clear that the sudden change in the pressure field, together with the vortices generated by the sail and aft appendages, will impact the wake structure and hence the operating conditions of the propeller.

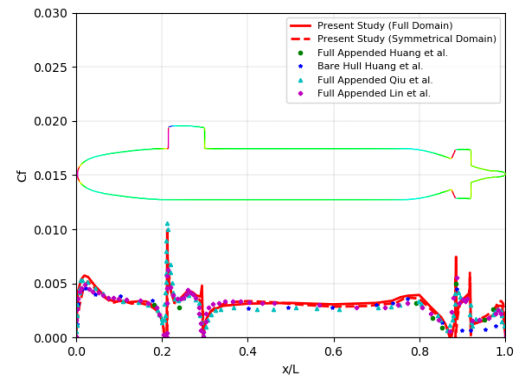


Fig. 14. Comparison of simulated and experimental results for the friction coefficient C_f along the top meridian line of the fully appended SUBOFF model.

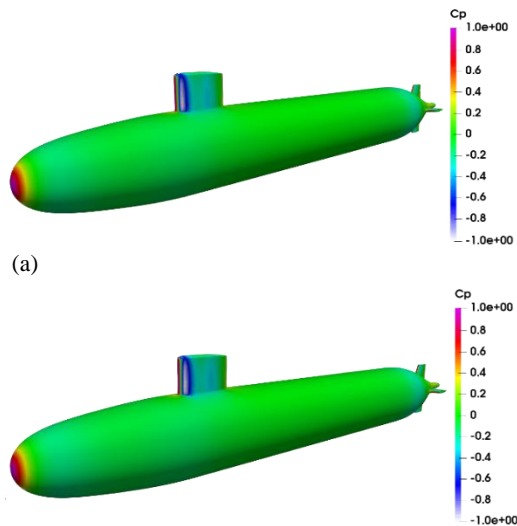


Fig. 15. Distributions of the pressure coefficient C_p in the SUBOFF model for (a) the full domain; (b) the symmetrical domain.

Figure 16 compares our results for the pressure coefficient C_p of the SUBOFF model along the upper midline line with experimental and other simulation results. The simulation results show that At the stagnation point ($x/L = 0$), C_p reaches its maximum and then quickly drops before reaching the point $x/L = 0.04$. C_p has a local peak at the upper midline at the sail's leading edge. ($x/L = 0.21$) and subsequently undergoes a sudden drop at the rear of the tripwire.

Because the sail's wake influences the pressure before $x/L = 0.4$, C_p tends to vary in the range $0.4 < x/L < 0.7$. A significant pressure gradient appears near the stern ($0.7 < x/L < 0.88$) and afterwards reaches a peak in front of the rudders. The interaction between the boundary layers and the rudders undoubtedly influences the change in C_p at the stern ($0.7 < x/L < 0.88$).

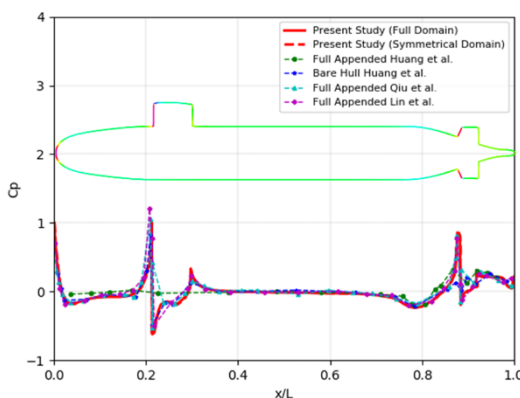


Fig. 16. Comparison of simulated and experimental results for the pressure coefficient C_p along the top meridian line of the fully appended SUBOFF model.

4. CONCLUSION

A detailed analysis of the effects of using full and symmetrical domains on the numerical flow around a SUBOFF submarine model has been presented in this paper. The flow was numerically modelled as single-phase and incompressible using OpenFOAM. To solve for the boundary layer near the wall, $k - \omega SST$ turbulence was used in both domains, together with an insensitive wall function. An uncertainty analysis was performed using a grid convergence test to verify both the accuracy of the solver and the convergence of the solution. Based on the discussions in this paper's preceding sections, we can summarise the following results as conclusions of our study:

- 1) Both the full and symmetrical domains were able to accurately predict the total resistance compared to experimental data.
- 2) Relative to the experimental results, the resistance value obtained from the symmetrical domain under the coarse grid condition had an error value of 1.34%, whereas the results for the full domain with the same grid size had an error value of 0.6%. Hence, the full domain is superior in terms of predicting the resistance with a coarse grid.
- 3) A comparison of the pressure coefficient at the leading edge of the rudder, where $x/L = 0.92$, revealed that the value for the symmetric domain was 0.0747, whereas the value for the full domain was 0.236. When compared to the pressure coefficient from experiment ($C_p = 0.302$), the symmetric domain appears to underestimate the pressure distribution at this position.
- 4) The flow structures arising from the sail and rudders differ between the full and symmetrical domains, and this is particularly true for the vortical structures.
- 5) The results from the full domain reveal that the flow around the SUBOFF model is asymmetric, and this model captures the features of the flow in more detail than the symmetrical domain.
- 6) The full domain captures the velocity distribution at the propeller plane better than the symmetrical domain. Hence, the full domain must be considered in an analysis of the propeller and self-propulsion simulation.

References

- Atta, T., Z. Ali, S. F. Ali and E. Uddin (2019). Hydrodynamic design and performance analysis of underwater vehicles using CFD. *Central European Symposium on Thermophysics 2019 (CEST)*.
- Barth, T. J. and D. C. Jespersen (1989). The design and application of upwind schemes on unstructured meshes. *27th Aerospace Sciences Meeting*.

- Boache, J. (1994). Perspective: A method for uniform reporting of grid refinement studies. *Journal of Fluid Engineering* 116, 405-413.
- Catalano, P., W. Meng, G. Iaccarino and P. Moin (2003). Numerical simulation of the flow around a circular cylinder at high Reynolds numbers. *International Journal of Heat and Fluid Flow* 24(4), 463-69.
- Constantinescu, G. and K. Squires (2004). Numerical investigations of flow over a sphere in the subcritical and supercritical regimes. *Physics of Fluids* 16(5), 1449-66.
- Doğrul, A. (2019). Hydrodynamic investigation of a submarine moving under free surface. *Journal of ETA Maritime Science* 7(3), 212-27.
- Ellis, C. L., D. B. Clarke, D. Butler and P. Brandner (2016). Complementary CFD study of generic submarine model tests in a cavitation tunnel. In *20th Australasian Fluid Mechanics Conference (20AFMC)* (pp. 1-4).
- Gao, W., N. Daniel, L. Zhenxia and L. Yaguo (2018). Numerical investigation of flow around one finite circular cylinder with two free ends. *Ocean Engineering* 156, 373-80.
- Huang, T., H. Liu, N. Groves, T. Forlini, J. Blanton and S. Growing (1992). Measurements of flows over an axisymmetric body with various appendages in a wind tunnel: The DARPA SUBOFF experimental program. In *Proceedings of the 19th Symposium on Naval Hydrodynamics*, Seoul, Korea.
- Islam, H. and C. G. Soares (2019). Uncertainty analysis in ship resistance prediction using OpenFOAM. *Ocean Engineering* 191, 105805.
- ITTC (2011). Practical guidelines for ship cfd applications. In *ITTC—Recommended Procedures and Guidelines, 26th ITTC Executive Committee*, Rio de Janeiro, Brazil, Chapter 7.5-03-02-03.
- ITTC (2017). Uncertainly analysis in CFD verification and validation methodology and procedures. In *ITTC—Recommended Procedures and Guidelines; 28th ITTC Executive Committee*. Chapter 7.5-03-01-01.
- ITTC (2021). Guideline for VIV Testing. In *ITTC—Recommended Procedures and Guidelines*. In *Ocean Engineering Committee of the 29th ITTC: France in Virtual*. Chapter 7.5-02-03-10.
- Lin, H. and C. Li (2020). The investigation of a sliding mesh model for hydrodynamic analysis of a SUBOFF model in turbulent flow fields. *Journal of Marine Science and Engineering* 8(10), 1-19.
- Lungu, A. (2019). DES-based computation of the flow around the DARPA SUBOFF. In *IOP Conference Series: Materials Science and Engineering*, Institute of Physics Publishing.
- Menter, R. (1994). Two-equation eddy-viscosity turbulence models for engineering applications. *AIAA Journal* 32(8), 1598-1605.
- Pan, Y., H. Zhang and Q. Zhou (2012). Numerical Prediction of Submarine Hydrodynamic Coefficients using CFD Simulation. *Journal of Hydrodynamics* 24(6), 840-847.
- Pantokratoras, A. (2017). Progress in Computational Fluid Dynamics. *Steady Flow of Power-Law Fluids across a Circular Rotating Cylinder*.
- Paredes, J., T. Maria, H. Quintuña and R. Datla (2021). Numerical flow characterization around a Type 209 submarine using OpenFOAM. *Fluids* 6(2).
- Paudel, S. and N. Saenger (2017). Grid refinement study for three dimensional CFD model involving incompressible free surface flow and rotating object. *Computers and Fluids* 143, 134-40.
- Pereira, S., G. Vaz, L. Eça, and S. Girimaji (2018). Simulation of the flow around a circular cylinder at Re=3900 with partially-averaged Navier-Stokes equations. *International Journal of Heat and Fluid Flow* 69, 234-46.
- Permadi, N. V. A. and E. Sugianto (2022). CFD Simulation Model for Optimum Design of B-Series Propeller using Multiple Reference Frame (MRF). *CFD Letters* 14(11), 22-39.
- Pook, D. A., D. B. Clarke, M. Jones, H. Quick and D. Ranmuthugala (2018, December). RANS based CFD prediction of submarine hydrodynamic loads. In *21st Australasian Fluid Mechanics Conference*, Adelaide, Australia.
- Qiu, Y., K. Shi, X. Hou and F. Wei (2007). Validation of numerical simulation of the flow over submarine geometries with full appendages. *Chuanbo Lixue Journal of Ship Mechanics* 11, 341-350.
- Rajani, N., A. Kandasamy and S. Majumdar (2009). Numerical simulation of laminar flow past a circular cylinder. *Applied Mathematical Modelling* 33(3), 1228-47.
- Roache, J. (1997). Quantification of uncertainty in computational fluid dynamics. *Annual review of fluid Mechanics* 29(1), 123-160.
- Roache, J. (1998). Verification of codes and calculations. *AIAA Journal* 36(5), 696-702.
- Rocha, A. L., L. Eça and G. Vaz (2017). On the numerical convergence properties of the

- calculation of the flow around the KVLCC2 tanker in unstructured grids. In *MARINE VII: proceedings of the VII International Conference on Computational Methods in Marine Engineering* (pp. 336-352). CIMNE.
- Roy, J. (2005). Review of code and solution verification procedures for computational simulation. *Journal of Computational Physics* 205(1), 131-56.
- Sadikin, A., Y. Nurul, K. Abdullah and M. Mohammed (2014). Numerical study of flow past a solid sphere at moderate Reynolds number. In *Applied Mechanics and Materials*, Trans Tech Publications Ltd.
- Sugianto, E., J. H. Chen and N. V. A. Permadi (2022). Effect of monohull type and catamaran hull type on ocean waste collection behavior using OpenFOAM. *Water* 14(17), 2623.
- Takahashi, K. and S. Prasanta (2019). Fundamental CFD Study on the hydrodynamic performance of the DARPA SUBOFF submarine. In *Volume 2: CFD and FSI*, American Society of Mechanical Engineers.
- Toxopeus, S. (2008). Viscous-flow calculations for bare hull DARPA SUBOFF submarine at incidence. *International Shipbuilding Progress* 55(3), 227-51.
- Ueda, H. and O. Hinze (1975). Fine-structure turbulence in the wall region of a turbulent boundary layer. *Journal of Fluid Mechanics* 67(1), 125-43.
- Versteeg, H. K. and W. Malalasekera (2007). *An introduction to computational fluid dynamics - the finite volume method*.
- Yen, C. H., U. J. Hui, Y. Y. We, A. Sadikin, N. Nordin, I. Taib, K. Abdullah, A. N. Mohammed, A. Sapit and M. W. M. Razali (2017). Numerical study of flow past a solid sphere at high Reynolds number. *IOP Conference Series*. <https://doi.org/10.1088/1757-899x/243/1/012042>
- Yin, G. and M. C. Ong (2020). On the wake flow behind a sphere in a pipe flow at low Reynolds numbers. *Physics of Fluids* 32(10), 103605. <https://doi.org/10.1063/5.0017349>